

Bessel Vortices in Spin-Orbit-Coupled Binary Bose-Einstein Condensates with Zeeman Splitting

Huan-Bo Luo^a, B. A. Malomed^b, Wu-Ming Liu^c, Lu Li^{a,*}

^a*Institute of Theoretical Physics and Department of Physics, State Key Laboratory of Quantum Optics and Quantum Optics Devices, Collaborative Innovation Center of Extreme Optics, Shanxi University, Taiyuan 030006, China*

^b*Department of Physical Electronics, School of Electrical Engineering, Faculty of Engineering, Tel Aviv University, Tel Aviv 69978, Israel*

^c*Beijing National Laboratory for Condensed Matter Physics, Institute of Physics, Chinese Academy of Sciences, Beijing 100190, China*

Abstract

We present an analysis of stationary solutions for two-dimensional (2D) Bose-Einstein condensates (BECs) with the Rashba spin-orbit (SO) coupling and Zeeman splitting. By introducing the generalized momentum operator, the linear version of the system can be solved exactly. The solutions are semi-vortices of the Bessel-vortex (BV) and modified Bessel-vortex (MBV) types, in the presence of the weak and strong Zeeman splitting, respectively. The ground states (GSs) of the full nonlinear system are constructed with the help of a specially designed neural network (NN). The GS of the mixed-mode type appears as cross-attraction interaction increases. The spin texture of the GS is produced in detail. It exhibits the Néel skyrmion structure for the semi-vortex GS of the BV type, and the respective skyrmion number is found in an analytical form. On the other hand, GSs of the MBV and mixed-mode types do not form skyrmions.

Keywords: Bessel vortices, Spin-orbit coupling, Zeeman splitting, Neural network

*Corresponding author.

Email address: 11z@sxu.edu.cn (Lu Li)

1. Introduction

Atomic Bose-Einstein condensates (BECs) are perfectly controllable quantum settings, which make it possible to emulate various effects which are well known in condensed-matter systems [1, 2]. A well-known example is the spin-orbit (SO) coupling in semiconductors, originating from the interaction of the electron spin with the weak magnetic field induced as the Lorentz transform of the electrostatic field of the crystalline lattice in the reference frame moving along with the electron. The solid-state SO coupling plays a fundamental role in the realization of spin Hall effects [3], topological insulators [4], spintronic devices [5], etc. There are two standard forms of the Hamiltonian of the SO coupling, viz., ones of the Dresselhaus [6] and Rashba [7, 8] types.

The last decade has witnessed the experimental realization of the emulation of the SO coupling in effectively one- [9, 10] and two-dimensional (2D) [11] BEC, see also reviews of the experimental and theoretical results in Refs. [12, 13, 14, 15]. Simultaneously, using Gross-Pitaevskii equations modeling the system [16], many remarkable effects have been predicted in SO-coupled BECs with intrinsic nonlinearity. These include vortices [17, 18, 20, 19], skyrmions [20] and many species of 1D [21, 22, 23, 24], 2D [25, 26, 27, 28, 29, 30, 31], and 3D [32] solitons, see also review [33]. Further, the SO coupling makes it possible to predict novel states of matter, such as chiral supersolids [34] and polariton topological insulators [35].

In this paper, we investigate stationary solutions for binary BEC with the SO coupling and Zeeman splitting between its two components. Starting from exact solutions of the linear version of the SO-coupled Gross-Pitaevskii equations, represented by Bessel vortices (BV) and modified Bessel vortices (MBV) in the presence of weak and strong Zeeman effects, respectively, we develop a neural network (NN) for simulating the system with the intrinsic attractive nonlinearity. The NN based numerical method [36, 37] is inherently parallel and even large-scale system can easily get accelerated with the modern Artificial Intelligence based computer. In this study, both the ground and excited states can be obtained by NN. In particular, the NN solutions produce 2D (“baby” [38, 39, 40]) skyrmions in the SO-coupled BEC (note that a baby skyrmion in a three-component condensate was created experimentally [41]). The corresponding values of the skyrmion number can be calculated analytically. Stability of the so predicted states is checked by dint of numerical simulations.

We consider a binary SO-coupled ${}^7\text{Li}$ BEC with attractive contact inter-

action and the Zeeman splitting between its components in the 2D space. SO coupling is created by laser beams which couple different states of ${}^7\text{Li}$ atoms [42]. The spinor wave function, $\Psi = (\Psi_1, \Psi_2)^T$, of this system is governed by the system of Gross-Pitaevskii equations. The scaled form of these equations is [26, 43]

$$\begin{aligned} i\partial_t\Psi_1 &= -\frac{1}{2}\nabla_{\perp}^2\Psi_1 + \beta[(\partial_x - i\partial_y)\Psi_2 + k_z\Psi_1] - (g|\Psi_1|^2 + \gamma|\Psi_2|^2)\Psi_1, \\ i\partial_t\Psi_2 &= -\frac{1}{2}\nabla_{\perp}^2\Psi_2 + \beta[-(\partial_x + i\partial_y)\Psi_1 - k_z\Psi_2] - (\gamma|\Psi_1|^2 + g|\Psi_2|^2)\Psi_2, \end{aligned} \quad (1)$$

and the characteristic length, energy and time are defined by $l = 2\mu\text{m}$, $\epsilon = \hbar^2/ml^2 = 2.4 \times 10^{-31}\text{J}$ and $\tau = \hbar/\epsilon = 0.44\text{ms}$ [43], where $m = 1.16 \times 10^{-26}\text{kg}$ is the mass of ${}^7\text{Li}$. The operator ∇_{\perp}^2 acts in the 2D plane (x, y) . The coefficient $\beta = 1$ is the SO coupling strength which can be varied in a broad range depending on laser configurations [42]. $g = 1$ and $\gamma = a_{\gamma}/a_g$ are coefficients of the self- and cross-attraction interaction, respectively. a_g and a_{γ} are the s -wave scattering lengths between atoms in same states and different states. In order to maintain the generality of the system, both a_g and a_{γ} can be varied in this system. The total number of atoms $U = (N/a_g)\sqrt{\hbar/8\pi m\omega_z}$, where $N = \int \Psi^{\dagger}\Psi dx dy$ is the norm integral and $\omega_z = 800\text{Hz}$ [44] is the frequency of tight confinement along the z axis. The Zeeman-splitting strength is $\Omega = \mu_B g_F B/\epsilon = \beta k_z$, where k_z may be considered as the z component of the momentum, g_F is the Landé g factor for ${}^7\text{Li}$, μ_B is the Bohr magneton and B is a uniform magnetic field in z axis. We can find that only k_z and γ are free parameters of the system.

Stationary solutions of Eq. (1) with chemical potential μ are sought for in the usual form,

$$\Psi = \{\psi_1(x, y), \psi_2(x, y)\}^T \exp(-i\mu t). \quad (2)$$

with stationary functions $\psi_{1,2}(x, y)$ satisfying equations

$$\begin{aligned} \mu\psi_1 &= -\frac{1}{2}\nabla_{\perp}^2\psi_1 + (\partial_x - i\partial_y)\psi_2 + k_z\psi_1 - (|\psi_1|^2 + \gamma|\psi_2|^2)\psi_1, \\ \mu\psi_2 &= -\frac{1}{2}\nabla_{\perp}^2\psi_2 - (\partial_x + i\partial_y)\psi_1 - k_z\psi_2 - (\gamma|\psi_1|^2 + |\psi_2|^2)\psi_2, \end{aligned} \quad (3)$$

In the presence of the Zeeman splitting, Eq. (3) yields two uniform states, *viz.*,

$$\psi_1 = C, \psi_2 = 0, \mu = k_z - C^2; \quad (4)$$

$$\psi_1 = 0, \psi_2 = C, \mu = -k_z - C^2, \quad (5)$$

where C is a real constant. In this paper, we only focus on the branch with lower chemical potential μ , as it is plausible that the higher branch is unstable. As concerns the uniform states, the lower branch corresponds to Eq. (5), in the case of $k_z > 0$.

A family of vortex solutions is defined by the ansatz [25, 26] which is compatible with the substitution of expression (2) in Eq. (1):

$$\psi_1(x, y) = R_1(r)e^{-i(m+1)\theta}, \psi_2(x, y) = R_2(r)e^{-im\theta}, \quad (6)$$

where (r, θ) are the polar coordinates, m is an integer winding number, and $R_{1,2}(r)$ are two radial wave functions. The simplest (fundamental) version of ansatz (6), corresponding to $m = 0$, or its mirror image with $m = -1$, represents the ground state (GS), in the form of the *semi-vortex*, as defined in Ref. [19] (see also review [45]), and the ones with *excitation number* $m \geq 1$ or $m \leq -2$ are defined, in the same works, as *excited states* of the semi-vortex unlike the GS, the excited states were found to be completely unstable (in the absence of the Zeeman splitting) [19], therefore only the GS solutions are considered here. Note that Eq. (1) is compatible with substitution $k_z \rightarrow -k_z$, $m \rightarrow -m - 1$, $R_1 \rightarrow -R_2$, $R_2 \rightarrow R_1$, therefore it is sufficient to consider only positive values of k_z .

2. Exact vortex states of the linearized system

First, we note that the stationary linear version of Eq. (1), i.e., $\hat{H}\psi = \mu\psi$ with Hamiltonian

$$\hat{H} = -\nabla_{\perp}^2/2 - (i\sigma_x\partial_y - i\sigma_y\partial_x - k_z\sigma_z), \quad (7)$$

where $\sigma_{x,y,z}$ are the Pauli matrices, admits an exact solution. Indeed, in terms of the generalized momentum operator,

$$\hat{P} = i\sigma_x\partial_y - i\sigma_y\partial_x - k_z\sigma_z, \quad (8)$$

Hamiltonian (7) can be written as $H = \hat{P}^2/2 - \hat{P} - k_z^2/2$. Then, solving the eigenvalue equation $\hat{P}\psi = k\psi$ with real k yields the exact solution of the linearized system (1), written in terms of the Bessel functions:

$$R_1(r) = Ck_r J_{m+1}(k_r r), R_2(r) = C(k + k_z) J_m(k_r r), \quad (9)$$

where C is an arbitrary real constant [similar to that in Eqs. (4) and (5)], k_r is the radial momentum, and the total momentum k is defined by

$$k^2 = k_r^2 + k_z^2. \quad (10)$$

The solution is built as a pair of the Bessel Vortices (BV) with winding numbers $-(m+1)$ and $-m$ in the ψ_1 and ψ_2 components, respectively. In the absence of the Zeeman effect, i.e., $k_z = 0$, this solution reduces to one that was recently reported in Ref. [46]. Naturally, the norm integral for this linear state in the free space diverges as

$$N \equiv N_1 + N_2 = \lim_{R \rightarrow \infty} \left\{ 2\pi \int_0^R [R_1^2(r) + R_2^2(r)] r dr \right\} \simeq 4C^2 \frac{k(k+k_z)}{k_r} R. \quad (11)$$

while the ratio of the norms of the two components is finite:

$$N_1/N_2 = k_r^2 / (k+k_z)^2. \quad (12)$$

Because operator \hat{P} , defined by Eq. (8), commutes with \hat{H} , the state ψ given by Eq. (9) is also the eigenstate of \hat{H} , with the respective chemical potential

$$\mu(k) = k^2/2 - k - k_z^2/2, \quad (13)$$

where the three terms represent, severally, the kinetic energy, SO coupling, and Zeeman energy shift. In the case of $k_z < 1$, the chemical potential attains its minimum,

$$\mu_{\min}(k_z < 1) = -1/2 - k_z^2/2, \quad (14)$$

at $k = 1$, hence Eq. (10) gives, in this case,

$$k_r = \sqrt{1 - k_z^2}. \quad (15)$$

In the limit of $k_z = 1$ and $k_r = 0$, the BV solution (9) amounts to the uniform state, with $R_1 = 0$, $R_2 = 2C$ for $m = 0$, and to zero solution for $m \geq 1$.

At $k_z > 1$, Eq. (15) yields an imaginary radial momentum k_r , and the BV solution (9) becomes the *modified Bessel Vortex* (MBV)

$$R_1 = -C|k_r|K_{m+1}(|k_r|r), R_2 = C(k+k_z)K_m(|k_r|r), \quad (16)$$

where K_m is the standard modified Bessel function of the second kind (alias the modified Hankel function), which exponentially decays at $r \rightarrow \infty$,

$$K_m(|k_r|r) \underset{r \rightarrow \infty}{\approx} \sqrt{\frac{\pi}{2|k_r|r}} \exp(-|k_r|r) \quad (17)$$

but is singular at $r \rightarrow 0$,

$$K_m(|k_r|r) \underset{r \rightarrow 0}{\approx} \frac{1}{2} (|m| - 1)! \left(\frac{2}{|k_r|r} \right)^{|m|} \quad (18)$$

for $m \geq 1$, and

$$K_0(|k_r|r) \underset{r \rightarrow 0}{\approx} \ln \left(\frac{2}{|k_r|r} \right). \quad (19)$$

Accordingly, the norm (11) of the MBV solutions of the linearized system diverges at $r \rightarrow 0$ as $r^{-2(m+1)}$ for $m \geq 1$, and as $\ln(1/r)$ for $m = 0$, while the ratio of the norms of the two components vanishes in the same limit.

As shown below, taking into account the self-attractive nonlinearity in Eq. (3) makes it possible to replace the GSs of the BV and MBV states by similar ones, but with a finite norm. Note that the nonlinearity does not affect the exponentially decaying asymptotic expression (17).

Finally, in the case of $k_z > 1$, the minimum value of the chemical potential is achieved at $k_r = 0$, hence Eqs. (10) and (13) yield

$$\mu_{\min}(k_z > 1) = -k_z. \quad (20)$$

The results show that, with the increase of the Zeeman-splitting strength k_z , the minimum chemical potential, given by Eq. (14), decreases, as per Eqs. (14) and (20), and the corresponding wave function carries over from the BV state ($0 \leq k_z < 1$) to the MBV one ($k_z > 1$). This is, in fact, an example of the quantum phase transition, as it occurs in terms of the mean-field wave function of the quantum gas, cf. Refs. [47, 48, 49]. A similar phase transition between BV and MBV localized states, with finite norms, is reported below. Note that all the vortex states are degenerate with respect to the excitation number m , as μ , given by Eq. (13), does not depend on m .

3. Constructing nonlinear vortex states by means of the neural network

Based on the exact vortex states found for the linear version, we aim to construct their nonlinear counterparts, as solutions of Eq. (1), with the help of a neural network (NN). First, we consider the case of $\gamma = 0$ [no nonlinear interaction between the components of the wave function in Eq. (1)]. Substituting the general ansatz (6) in Eq. (1) with $\gamma = 0$ yields

$$G_{1,2}(r, R_1, R'_1, R''_1, R_2, R'_2, R''_2) = 0, \quad (21)$$

where

$$\begin{aligned} G_1 &= (-\mu + k_z) R_1 - \frac{1}{2} \left[R_1'' + \frac{R_1'}{r} - \frac{(m+1)^2 R_1}{r^2} \right] + R_2' - \frac{m R_2}{r} - R_1^3, \\ G_2 &= (-\mu - k_z) R_2 - \frac{1}{2} \left[R_2'' + \frac{R_2'}{r} - \frac{m^2 R_2}{r^2} \right] - R_1' - \frac{(m+1) R_1}{r} - R_2^3. \end{aligned} \quad (22)$$

Next, introducing the error index,

$$L \equiv 2\pi \int_0^\infty r (G_1^2 + G_2^2) dr, \quad (23)$$

the task is to drive its value to zero as close as possible for given chemical potential μ .

In the nonlinear system, localized solutions may exist in the *bandgap* of the linear spectrum of Eq. (3), i.e., at values of μ at which the linear solutions (9) and (16) do not exist, cf. Ref. [26]. As it follows from Eqs. (14) and (20), the bandgap is

$$\mu < \begin{cases} -1/2 - k_z^2/2, & \text{at } k_z < 1, \\ -k_z, & \text{at } k_z > 1. \end{cases} \quad (24)$$

It is shown by the yellow area in the plane of (k_z, μ) , in Fig. 1(b). Thus, the chemical potential of localized states can be denoted as

$$\mu = \mu_{\min} - \Delta, \quad \text{with } \Delta > 0. \quad (25)$$

As the self-focusing nonlinearity can chop off the slowly decaying tails of the Bessel wave function, which makes its norm integral norm diverging [see Eq. (11)], we adopt the following ansatz, which agrees with the general structure of the BV solutions (9) and includes the truncation factor $\text{sech}(ar)$:

$$R_1 = o_1 \text{sech}(ar) J_{m+1}(o_3 r), \quad R_2 = o_2 \text{sech}(ar) J_m(o_4 r), \quad (26)$$

where $a = \sqrt{2\Delta}$ is an empirical choice, suggested by numerical computations [recall Δ is defined by Eq. (25)]. Both BV and MBV states can be produced by the input taken as per ansatz (26).

A schematic of the NN used in this study is shown in Fig. 1(a). It includes three layers, *viz.*, an input one $X = [1, r]^T$, hidden layer $H_l = [1, h_1, h_2, h_3, \dots, h_n]^T$, and the output one, $O = [o_1, o_2, o_3, o_4]^T$. The appended “1” in X and H_l is used to account for the bias in the input and

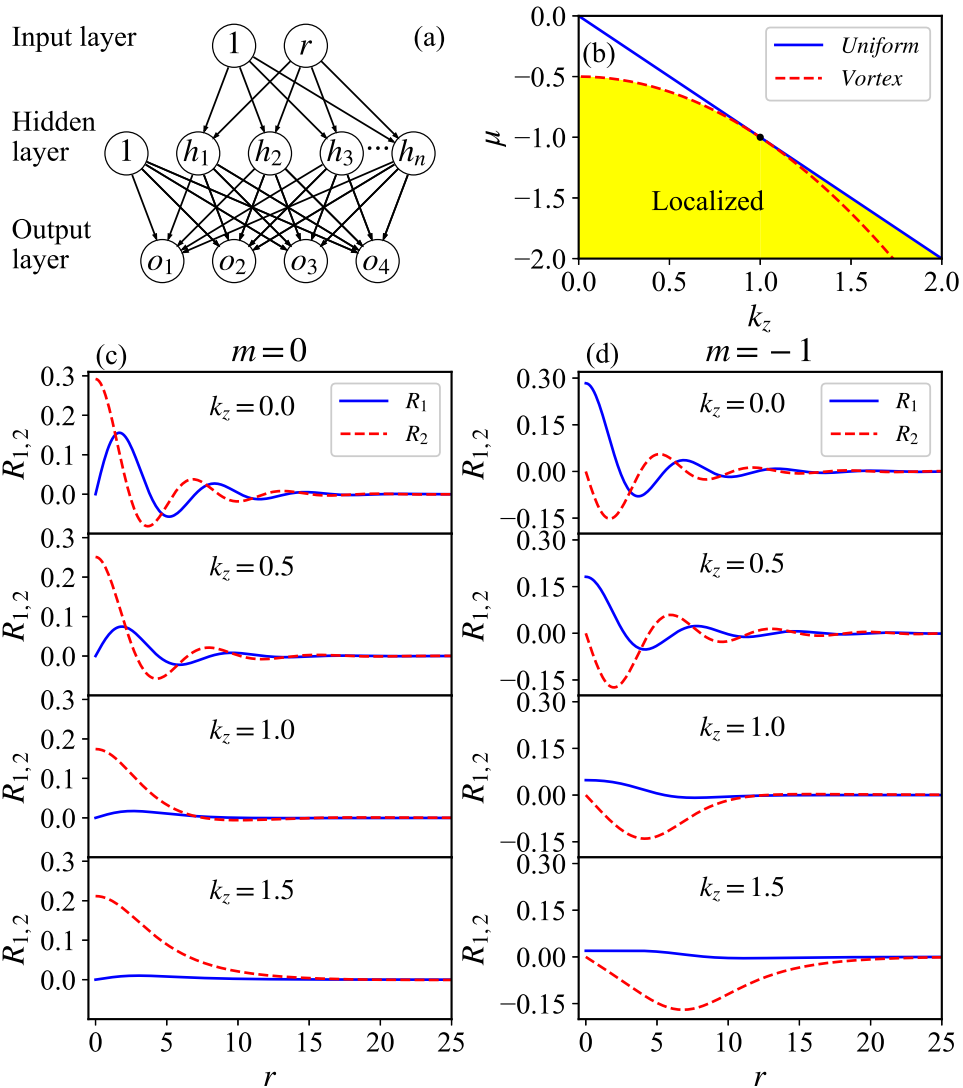


Figure 1: (Color online) (a) The schematic of the NN with $1 + 1$ input nodes, $1 + n$ hidden nodes, and 4 output nodes. (b) The linear dispersion spectrum of the system. Localized states exist in the yellow area. Profiles of the radial wave functions $R_{1,2}$ are displayed in panels (c) for $m = 0$ and (d) for $m = -1$, at $k_z = 0.0, 0.5, 1$ and 1.5 . Here $\Delta = 0.01$ [see Eq. (25)].

hidden layer. The bias has the effect of shifting the activation function by a constant, which can improve the accuracy of output generated by the NN. The hidden and output layers can be expressed as

$$H_l = [1, f(WX)^T]^T, O = Af(VH_l), \quad (27)$$

where W and V are $2 \times n$ and $(n + 1) \times 4$ parameter matrices. Here, we choose $n = 12$ and $A = 2$, initial values of W and V are given by random numbers uniformly distributed between -1 and $+1$, and $f(x) = 1/(1+e^{-x})$ is a component-wise sigmoid activation function. A component-wise function $y = f(x)$ can be defined as that if x is matrix, then $y_{ij} = f(x_{ij})$. Thus, for given W and V , we can obtain an error index $L(W, V)$ and its gradient with respect to W and V . Based on the gradient, the parameter matrices W and V can be updated by means of the adaptive-moment estimation (Adam) method. Note that this method cannot avoid producing the trivial solution, $R_1 = R_2 = 0$, of Eq. (21). In that case, the total norm quickly decays toward zero, and we then need to generate a new set of W and V for the next iteration. The soliton solution can be found if the total norm becomes a constant instead of decaying to zero.

As mentioned above, we focus on the consideration of the GSs, which are represented by ansatz (9) with $m = 0$ and -1 . The BV ($0 \leq k_z < 1$) and MBV ($k_z > 1$) states with $m = 0, -1$ were calculated at $\Delta = 0.01$, as shown in Figs. 1(c-d). It takes about 3×10^4 iterations to reduce values of the error index (23) to $L < 10^{-6}$. Naturally, the radial wave functions of the BV states feature the oscillatory decaying tail, while the oscillations are absent in the MBV states. Because the presence or absence of the oscillations in the tails of the localized states is the indicator of the quantum phase transition between ones of the BV and MBV types, $k_z = 1$ remains the phase-transition point, exactly the same as in the linear system considered above. It is relevant to mention that, although the system (1) dealt with here is similar to one addressed in Ref. [26], the BV \rightarrow MBV phase transition at $k_z = 1$ was not considered in that work. Profiles of the o_{1-4} functions generated by NN, as intermediate results, are shown in Fig. 2.

The total norm N of the so obtained solutions are plotted, vs. Δ , in Figs. 3(a,c). The stability of the stationary solutions can be identified through the computation of eigenvalues for small perturbations added, in the linear approximation, to the stationary states. It has thus been checked that all the GS solutions obtained in this work [for $\gamma = 0$ in Eq. (1)] are stable.

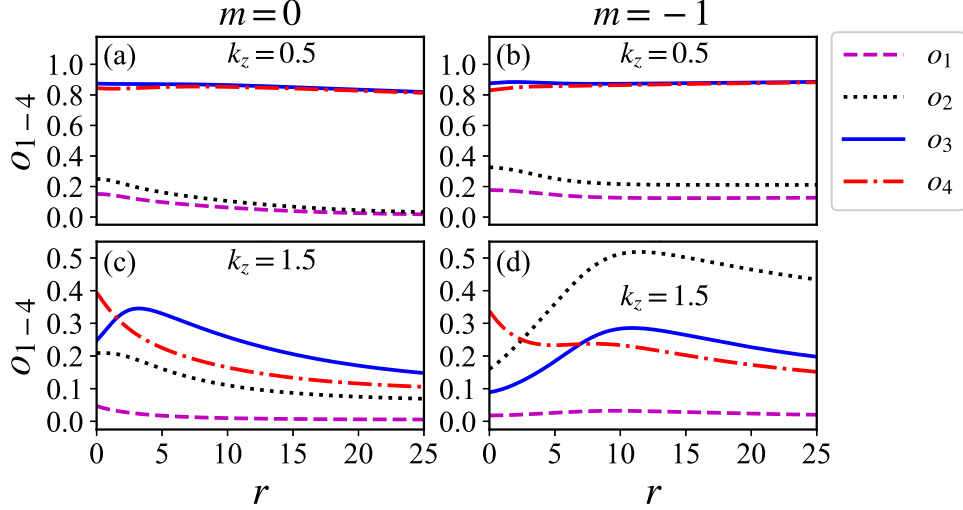


Figure 2: (Color online) Profiles of the o_{1-4} functions generated by NN are displayed in panels (a,c) for $m = 0$ and (b,d) for $m = -1$, at $k_z = 0.5$ and 1.5 . Here $\Delta = 0.01$

The true GS of the system can be identified by calculating the energy corresponding to Eq. (1),

$$\begin{aligned}
 E = \iint \left\{ \frac{1}{2} (|\nabla\psi_1|^2 + |\nabla\psi_2|^2) + \psi_1^* (\partial_x - i\partial_y) \psi_2 - \psi_2^* (\partial_x + i\partial_y) \psi_1 \right. \\
 \left. + k_z (|\psi_1|^2 - |\psi_2|^2) - \frac{g}{2} (|\psi_1|^4 + |\psi_2|^4) - \gamma |\psi_1|^2 |\psi_2|^2 \right\} dx dy, \quad (28)
 \end{aligned}$$

where $*$ stands for the complex conjugate. From Figs. 3(b,d) it is seen that energy of the BV and MBV states with $m = 0$ is always lower than that of their counterparts with $m = -1$, which means that the state with $m = 0$ represent the GS. Thus, the introduction of the Zeeman splitting lifts the degeneracy between the states with $m = 0$ and -1 [19].

Further, ratio N_1/N_2 of the norms of the ψ_1 and ψ_2 components of the GS with $m = 0$ is plotted in Fig. 3(e). It is close to the same ratio found for the exact solutions of the linearized equations, given by Eq. (12) at $\Delta = 0.01$. The two-component Bose gas can be considered as a (pseudo-)spin system. The spin vector, $\mathbf{S} = \psi^\dagger \boldsymbol{\sigma} \psi / \psi^\dagger \psi$, can be used to represent the respective pseudo-magnetic ordering, where $\boldsymbol{\sigma} = (\sigma_x, \sigma_y, \sigma_z)$ is the Pauli matrix vector. The average z -component of the spin $\bar{S}_z = \langle \psi | \sigma_z | \psi \rangle / N = (N_1/N_2 - 1)/(N_1/N_2 + 1)$, and the magnetization is defined as $M = |\bar{S}_z|$. Note that $M = k_z$ for $0 \leq k_z < 1$ in linear regime. The magnetization curve

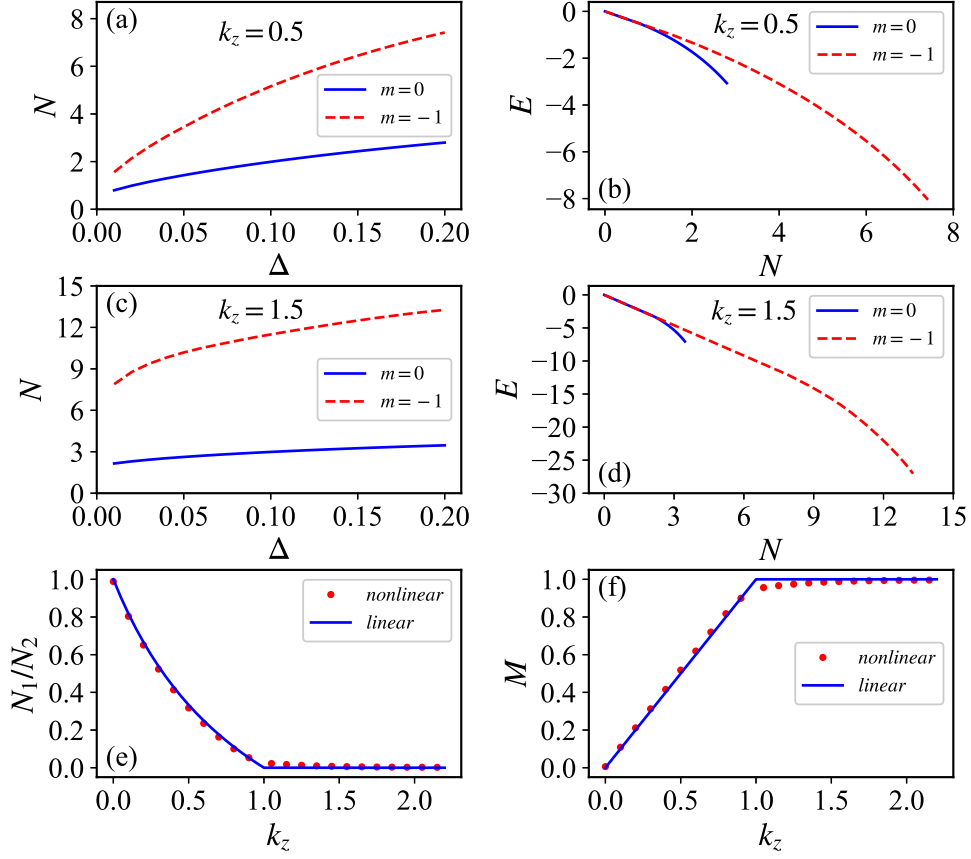


Figure 3: (Color online) The total norm N as a function of Δ [see Eq. (25)] for the states with $m = 0$ and -1 and (a) $k_z = 0.5$ and (c) $k_z = 1.5$. The corresponding total energy (28) for (b) $k_z = 0.5$ and (d) $k_z = 1.5$. (e) Ratio N_1/N_2 and (f) the magnetization curve for the system's GS with $m = 0$. Here, the data points are calculated at $\Delta = 0.01$.

for $m = 0$ is plotted in Fig. 3(f). Without the external magnetic field applied to the BEC, i.e., at $k_z = 0$, the atoms are evenly distributed in the ψ_1 and ψ_2 components, i.e. $N_1/N_2 = 1$, hence the magnetization is negligibly small. With the increase of the external magnetic field k_z , the atomic population is transferred from ψ_1 to ψ_2 , which yields a higher magnetization. Eventually, at the critical value of the effective field, $k_z = 1$, nearly all the atoms are transferred to ψ_2 . The magnetization remains nearly constant as $k_z > 1$, which means saturation of the magnetization.

The above consideration was performed for $\gamma = 0$ in Eq. (1). In the presence of γ , i.e., the nonlinear interaction between the two components of the wave function, one may expect that the GS is represented not by the semi-vortex of the BV or MBV type, but by the mixed mode, in which both components contain mixtures of azimuthal harmonics with winding numbers 0 and ± 1 , cf. Eq. (6). Here, we consider the mixed modes, the initial guess for which is built as a superposition of semi-vortices of the BV or MBV types, with $m = 0$ and $m = -1$:

$$\begin{aligned}\psi_1 &= \text{sech}(ar) [o_1 e^{-i\theta} J_1(o_2 r) + o_3 J_0(o_4 r)], \\ \psi_2 &= \text{sech}(ar) [o_5 J_0(o_6 r) + o_7 e^{i\theta} J_{-1}(o_8 r)],\end{aligned}\tag{29}$$

cf. Eq. (26). The weight of each semi-vortex in this ansatz may be defined as

$$c_0 = d_0/(d_0 + d_{-1}), \quad c_{-1} = 1 - c_0,\tag{30}$$

where

$$\begin{aligned}d_0 &= \iint \text{sech}^2(ar) [o_1^2 J_1^2(o_2 r) + o_3^2 J_0^2(o_4 r)] dx dy, \\ d_{-1} &= \iint \text{sech}^2(ar) [o_5^2 J_0^2(o_6 r) + o_7^2 J_{-1}^2(o_8 r)] dx dy.\end{aligned}\tag{31}$$

are norms of both semivortex constituents. It follows from Eqs. (30) and (31) that weights c_0 and c_{-1} belong to the interval of $0 < c_0, c_{-1} < 1$.

Similar to the NN used above, parameters o_{1-8} from ansatz (29) can be determined by means of the NN employing the Adam method to minimize the error index, which is defined as

$$L \equiv \int_{-\infty}^{\infty} \int_{-\infty}^{\infty} (|G_1|^2 + |G_2|^2) dx dy,\tag{32}$$

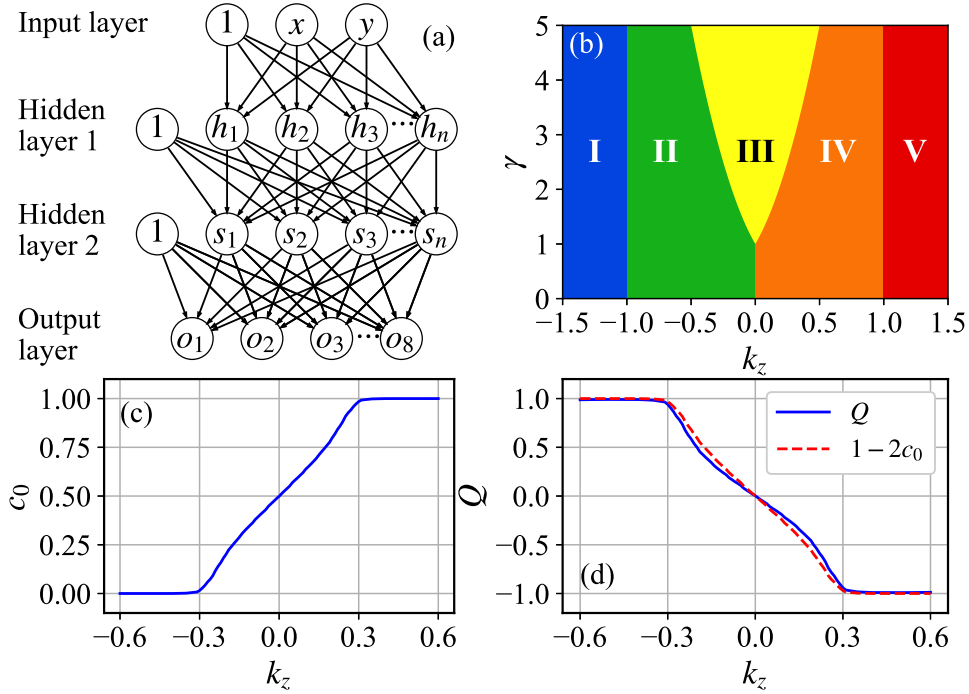


Figure 4: (Color online) The schematic of the NN with $2 + 1$ input nodes, two layers of $n + 1$ hidden nodes, and 8 output ones. (b) Diagram of the GS of the MBV semi-vortex type with (I) $m = -1$ and (V) $m = 0$; the GS of the BV semi-vortex type with (II) $m = -1$ and (IV) $m = 0$; and (III) the mixed-mode state in the (γ, k_z) plane. (c) The weight c_0 and (d) skyrmion number Q in the mixed mode as functions of k_z for $\gamma = 3$ in Eq. (1) and $\Delta = 0.1$, see Eq. (25).

cf. Eq. (23), where $G_{1,2}$ are defined as

$$\begin{aligned} G_1 &= \left(-\mu - \frac{1}{2} \nabla_{\perp}^2 \right) \psi_1 + (\partial_x - i\partial_y)\psi_2 + k_z\psi_1 - (|\psi_1|^2 + \gamma|\psi_2|^2) \psi_1, \\ G_2 &= \left(-\mu - \frac{1}{2} \nabla_{\perp}^2 \right) \psi_2 - (\partial_x + i\partial_y)\psi_1 - k_z\psi_2 - (\gamma|\psi_1|^2 + |\psi_2|^2) \psi_2, \end{aligned} \quad (33)$$

cf. Eq. (22). The schematic of the presently used NN is shown in Fig. 4(a). There are four layers, *viz.*, the input one $X = [1, x, y]^T$, the first and second hidden layers, $H_l = [1, h_1, h_2, h_3, \dots, h_n]^T$ and $S_l = [1, s_1, s_2, s_3, \dots, s_n]^T$, and output one $O = [o_1, o_2, o_3, o_4, \dots, o_8]^T$. The hidden and output layers can be written as

$$H_l = [1, f(W_1 X)^T]^T, S_l = [1, f(W_2 H_l)^T]^T, O = Af(V S_l). \quad (34)$$

where W_1 , W_2 , and V are $3 \times n$, $(n+1) \times n$ and $(n+1) \times 8$ parameter matrices, respectively.

The numerical calculation was performed for $\Delta = 0.1$ [see Eq. (25)]. After $\simeq 10^4$ iterations, the error index (32) is pushed down to $\sim 10^{-6}$. According to the distribution of weight parameter c_0 [see Eq. (30)], we plot the phase diagram of the GS in the (γ, k_z) parameter plane, as shown in Fig. 4(b), where I, II, IV and V correspond to the semi-vortex of the BV type, and III represents the mixed mode. We have found that, similar to Ref. [25], the mixed mode exists only at $\gamma > 1$, and the phase-transition curve between the mixed mode and semi-vortex of the BV type can be fitted by expression

$$\gamma = 8k_z^2 + 4|k_z| + 1. \quad (35)$$

As an example, Fig. 4(c) presents weight c_0 as a function of k_z at $\gamma = 3$, where the two phase transition points are $k_z = \pm 0.31$ (note that the respective value $|k_z| = 0.31$ is essentially smaller than $k_z = 1$ at which the $\text{BM} \rightarrow \text{MBV}$ phase transition occurs in the semi-vortices, as shown above). The corresponding density distributions in each component are shown in the first and second columns of Fig. 5. The prediction of spatial distribution of atoms for each component can be tested by the Stern-Gerlach experiment.

For the semi-vortex of the BV type, with excitation number m [see Eq. (6)], the spin vector produced by the linear solution is

$$\mathbf{S}_m = [\sin \Phi_m(r) \cos \theta, \sin \Phi_m(r) \sin \theta, \cos \Phi_m(r)], \quad (36)$$

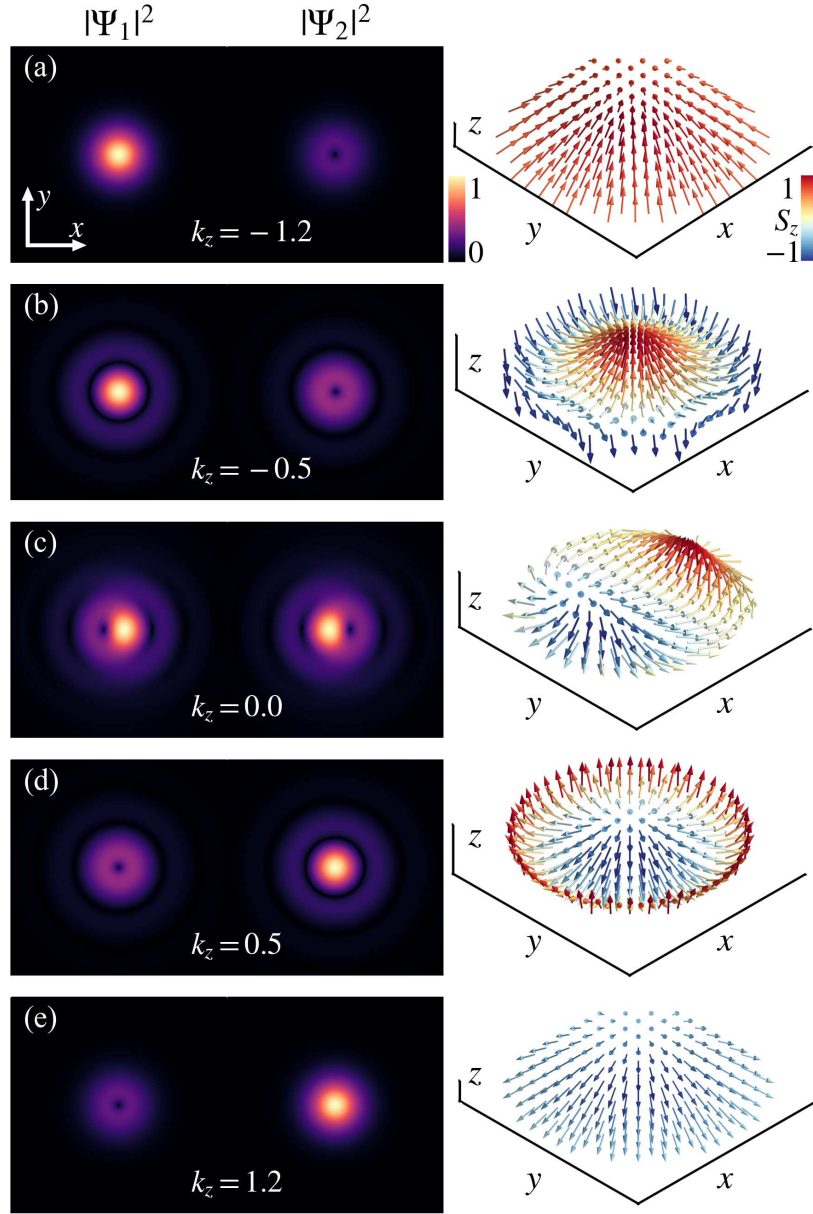


Figure 5: (Color online) Density distributions of the ψ_1 and ψ_2 components (the first and second columns, respectively). The third column displays the corresponding spin textures for $\gamma = 3$ and $\Delta = 0.1$. Arrows indicate the direction of the spin, and their colors represent the component orthogonal to the (x, y) plane, that is, the respective directions vary from vertical up (red) to vertical down (blue).

where

$$\sin \Phi_m(r) = 2R_1R_2 / (R_1^2 + R_2^2), \cos \Phi_m(r) = (R_2^2 - R_1^2) / (R_1^2 + R_2^2). \quad (37)$$

Note properties of this vector: $\mathbf{S}_m = -\mathbf{S}_{-m-1}$, and $\lim_{r \rightarrow 0} \Phi_m(r) = -\pi \text{sign}(m) = -\Phi(r_0)$, where r_0 is the minimal positive root of $R_1(r)R_2(r) = 0$ [and we set $\text{sign}(0) = 1$].

The SO coupling in the BEC Hamiltonian is tantamount to the Dzyaloshinskii-Moriya interaction, supporting topologically nontrivial spin textures, i.e., skyrmions [50]. This texture is characterized by the topological skyrmion number

$$Q = \frac{1}{4\pi} \iint_{\Sigma} \mathbf{S} \cdot \left(\frac{\partial \mathbf{S}}{\partial x} \times \frac{\partial \mathbf{S}}{\partial y} \right) dx dy, \quad (38)$$

where the integration domain is $\Sigma : 0 \leq r \leq r_0, 0 \leq \theta < 2\pi$, with r_0 defined above. The skyrmion number of the semi-vortex of the BV type with excitation number m is given by

$$Q_{SV}^{(m)} = (1/4\pi) \cos \Phi(r)|_{r=0}^{r=r_0} \theta|_{\theta=0}^{\theta=2\pi} = -\text{sign}(m). \quad (39)$$

The mixed mode can be considered as a weighted superposition of a skyrmion and an antiskyrmion (which is sometimes called ‘‘skyrmionium’’ [51]), thus the respective total skyrmion number is

$$Q_{MM} = c_0 Q_{SV}^{(0)} + c_{-1} Q_{SV}^{(-1)} = 1 - 2c_0. \quad (40)$$

The spin textures of the BV-semi-vortex and mixed-mode states are summarized in Fig. 5, where the above-mentioned boundary value is $r_0 = 2.40/\sqrt{1 - k_z^2}$ at $|k_z| < 1$. The spin textures of the BV semi-vortex exhibit the Néel skyrmion structure, while the MBV semi-vortex with $k_z > 1$ and mixed mode do not form skyrmions.

We have calculated the skyrmion number numerically, as shown in Fig. 4(d), where the skyrmion number is correctly approximated by Eq. (40). In particular, the fact that Q takes integer values ± 1 for semi-vortices of the BV type in areas II and IV of the figure agrees with the above-mentioned fact that only these modes form true skyrmions.

Lastly, all the GSs mentioned above are stable. This conclusion is confirmed by direct simulations, as well as by the computation of eigenvalues for small perturbations, cf. the stability analysis performed for 2D localized states in other models [26, 52, 53, 45].

Compared with the traditional numerical method (imaginary-time propagation method) for solving Gross-Pitaevskii equation, NN method has both advantages and disadvantages. In terms of efficiency, the NN method is time-consuming if there is no hardware acceleration. By employ a CPU (Intel Core i7-1165G7), NN method takes 28.3 hours to obtain a 2D solution, while traditional numerical method only takes 7.2 hour to obtain the same solution. However, NN method can be accelerated by a GPU (NVIDIA RTX-2060) so that the calculation time can be reduced to 2.4 hours. The greatest advantage of NN method is that both ground state and excited state can be obtained as long as the correct ansatzs are given, while the traditional numerical method can only obtain the ground state. However, it is difficult to give the correct ansatzs, especially for a unfamiliar system. Note that the ansatzs (26) and (29) given in this paper are based on the linear exact solution (9).

4. Conclusion

We have investigated stationary solutions in the 2D model of the binary BEC, including the SO (spin-orbit) coupling of the Rashba type and Zeeman splitting. By introducing the generalized momentum operator, the linear version of the system can be solved exactly. The solutions are a pair of the BVs (Bessel vortices) or MBVs (modified Bessel vortices), in the cases of the weak and strong Zeeman splitting, respectively. The corresponding stationary localized vortex solutions of the full nonlinear system are constructed by means of specially designed NN (neural network). While the system is similar to those addressed in earlier works, a new result is the exactly identified quantum phase transition between the semi-vortex GSs (ground states) of the BV and MBV types. In the presence of the nonlinear interaction between the two components of the wave function, the GS of the mixed-mode type is constructed too, by a pair of BV states with excitation numbers $m = 0$ and -1 , is also considered. The spin texture of the GS of the BV-semi-vortex type exhibits the Néel skyrmion structure, and its skyrmions number is calculated analytically, while the semi-vortices of the MBV type and mixed modes do not form skyrmions. All the GSs identified in this work are stable, which implies that they have the potential to be realized in the experiment. The analysis presented here may be readily extend to other SO-coupled systems, such as three-component BEC with the spin-1 composition.

This research was supported by 111 project (grant No. D18001), the Hundred Talent Program of the Shanxi Province (2018), the National Key R&D Program of China under grants No. 2021YFA1400900, 2021YFA0718300, 2021YFA1400243, NSFC under grants Nos. 61835013 and by the Israel Science foundation (grant No. 1286/17).

CRedit authorship contribution statement

Huan-Bo Luo: Methodology, Writing - original draft. B. A. Malomed: Validation, Writing - review and editing. Wu-Ming Liu: Validation, Writing - review and editing. Lu Li: Conceptualization, Supervision, Writing - review and editing.

References

- [1] Hauke P, Cucchietti FM, Tagliacozzo L, Deutsch I, Lewenstein M. Can one trust quantum simulators? *Rep. Prog. Phys.* 2012;75. <https://doi.org/10.1088/0034-4885/75/8/082401>.
- [2] Lewenstein M, Sanpera A, Ahufinger V. *Ultracold Atoms in Optical Lattices: Simulating quantum many-body systems*. OUP Oxford; 2012.
- [3] Xiao D, Chang M-C, Niu Q. Berry phase effects on electronic properties. *Rev. Mod. Phys.* 2010;82. <https://doi.org/10.1103/RevModPhys.82.1959>.
- [4] Hasan MZ, Kane CL. Colloquium: Topological insulators. *Rev. Mod. Phys.* 2010;82. <https://doi.org/10.1103/RevModPhys.82.3045>.
- [5] Žutić I, Fabian J, Sarma SD. Spintronics: Fundamentals and applications. *Rev. Mod. Phys.* 2004;76. <https://doi.org/10.1103/RevModPhys.76.323>.
- [6] Dresselhaus G. Spin-Orbit Coupling Effects in Zinc Blende Structures. *Phys. Rev.* 1955;100. <https://doi.org/10.1103/PhysRev.100.580>.
- [7] Bychkov YA, Rashba EI. Oscillatory effects and the magnetic susceptibility of carriers in inversion layers *J. Phys. C: Solid State Phys.* 1984;17. <https://doi.org/10.1088/0022-3719/17/33/015>.

- [8] Rashba EI, Sherman EYa. Spin-orbital band splitting in symmetric quantum wells. *Phys. Lett. A* 1988;129:175-179. [https://doi.org/10.1016/0375-9601\(88\)90140-5](https://doi.org/10.1016/0375-9601(88)90140-5).
- [9] Lin Y-J, Jiménez-García K, Spielman IB. Spin-orbit-coupled Bose-Einstein condensates. *Nature (London)* 2011;471:83-86. <https://doi.org/10.1038/nature09887>.
- [10] Anderson BM, Juzeliūnas G, Galitski VM, Spielman IB. Synthetic 3D Spin-Orbit Coupling. *Phys. Rev. Lett.* 2012;108. <https://doi.org/10.1103/physrevlett.108.235301>.
- [11] Wu Z, Zhang L, Sun W, Xu X-T, Wang B-Z, Ji S-C, et al. Realization of two-dimensional spin-orbit coupling for Bose-Einstein condensates. *Science* 2016;354:83-88. <https://doi.org/10.1126/science.aaf6689>.
- [12] Spielman IB. Light Induced Gauge Fields for Ultracold Neutral Atoms. *Annual Review of Cold Atoms and Molecules*, World Scientific; 2013, p. 145-187.
- [13] Galitski V, Spielman IB. Spin-orbit coupling in quantum gases. *Nature (London)* 2013;494:49-54. <https://doi.org/10.1038/nature11841>.
- [14] Goldman N, Juzeliūnas G, Öhberg P, Spielman IB. Light-induced gauge fields for ultracold atoms. *Rep. Prog. Phys.* 2014;77:126401. <https://doi.org/10.1088/0034-4885/77/12/126401>.
- [15] Zhai H. Degenerate quantum gases with spin-orbit coupling: a review. *Rep. Prog. Phys.* 2015;78:026001. <https://doi.org/10.1088/0034-4885/78/2/026001>.
- [16] Zhang Y, Mao L, Zhang C. Mean-Field Dynamics of Spin-Orbit Coupled Bose-Einstein Condensates. *Phys. Rev. Lett.* 2012;108. <https://doi.org/10.1103/physrevlett.108.035302>.
- [17] Kawakami T, Mizushima T, Machida K. Textures of $F = 2$ spinor Bose-Einstein condensates with spin-orbit coupling. *Phys. Rev. A* 2011;84. <https://doi.org/10.1103/PhysRevA.84.011607>.

- [18] Ramachandran B, Opanchuk B, Liu X-J, Pu H, Drummond PD, Hu i H. Half-quantum vortex state in a spin-orbit-coupled Bose-Einstein condensate. *Phys. Rev. A* 2012;85. <https://doi.org/10.1103/PhysRevA.85.023606>.
- [19] Sakaguchi H, Li B. Vortex lattice solutions to the Gross-Pitaevskii equation with spin-orbit coupling in optical lattices. *Phys. Rev. A* 2013;87. <https://doi.org/10.1103/PhysRevA.87.015602>.
- [20] Kawakami T, Mizushima T, Nitta M, Machida K. Stable Skyrmions in $SU(2)$ Gauged Bose-Einstein Condensates. *Phys. Rev. Lett.* 2012;109. <https://doi.org/10.1103/PhysRevLett.109.015301>.
- [21] Achilleos V, Frantzeskakis DJ, Kevrekidis PG, Pelinovsky DE. Matter-Wave Bright Solitons in Spin-Orbit Coupled Bose-Einstein Condensates. *Phys. Rev. Lett.* 2013;110. <https://doi.org/10.1103/PhysRevLett.110.264101>.
- [22] Xu Y, Zhang Y, Wu B. Bright solitons in spin-orbit-coupled Bose-Einstein condensates. *Phys. Rev. A* 2013;87. <https://doi.org/10.1103/physreva.87.013614>.
- [23] Salasnich L, Malomed BA. Localized modes in dense repulsive and attractive Bose-Einstein condensates with spin-orbit and Rabi couplings. *Phys. Rev. A* 2013;87. <https://doi.org/10.1103/physreva.87.063625>.
- [24] Kartashov YV, Konotop VV, Abdullaev FK. Gap Solitons in a Spin-Orbit-Coupled Bose-Einstein Condensate. *Phys. Rev. Lett.* 2013;111. <https://doi.org/10.1103/PhysRevLett.111.060402>.
- [25] Sakaguchi H, Li B, Malomed BA. Creation of two-dimensional composite solitons in spin-orbit-coupled self-attractive Bose-Einstein condensates in free space. *Phys. Rev. E* 2014;89. <https://doi.org/10.1103/PhysRevE.89.032920>.
- [26] Sakaguchi H, Sherman EYa, Malomed BA. Vortex solitons in two-dimensional spin-orbit coupled Bose-Einstein condensates: Effects of the Rashba-Dresselhaus coupling and Zeeman splitting. *Phys. Rev. E* 2016;94. <https://doi.org/10.1103/PhysRevE.94.032202>.

- [27] Salasnich L, Cardoso WB, Malomed BA. Localized modes in quasi-two-dimensional Bose-Einstein condensates with spin-orbit and Rabi couplings. *Phys. Rev. A* 2014;90. <https://doi.org/10.1103/PhysRevA.90.033629>.
- [28] Lobanov VE, Kartashov YV, Konotop VV. Fundamental, Multipole, and Half-Vortex Gap Solitons in Spin-Orbit Coupled Bose-Einstein Condensates. *Phys. Rev. Lett.* 2014;112. <https://doi.org/10.1103/PhysRevLett.112.180403>.
- [29] Li Y, Liu Y, Fan Z, Pang W, Fu S, Malomed BA. Two-dimensional dipolar gap solitons in free space with spin-orbit coupling. *Phys. Rev. A* 2017;95. <https://doi.org/10.1103/PhysRevA.95.063613>.
- [30] Sakaguchi H, Malomed BA. One- and two-dimensional gap solitons in spin-orbit-coupled systems with Zeeman splitting. *Phys. Rev. A* 2018;97. <https://doi.org/10.1103/PhysRevA.97.013607>.
- [31] Kartashov YV, Torner L, Modugno M, Sherman EYa, Malomed BA, Konotop VV. Multidimensional hybrid Bose-Einstein condensates stabilized by lower-dimensional spin-orbit coupling. *Phys. Rev. Research* 2020;2. <https://doi.org/10.1103/PhysRevResearch.2.013036>.
- [32] Zhang Y-C, Zhou Z-W, Malomed BA, Pu H. Stable Solitons in Three Dimensional Free Space without the Ground State: Self-Trapped Bose-Einstein Condensates with Spin-Orbit Coupling. *Phys. Rev. Lett.* 2015;115. <https://doi.org/10.1103/PhysRevLett.115.253902>.
- [33] Malomed BA. Creating solitons by means of spin-orbit coupling. *EPL* 2018;122:36001. <https://doi.org/10.1209/0295-5075/122/36001>.
- [34] Han W, Zhang X-F, Wang D-S, Jiang H-F, Zhang W, Zhang S-G. Chiral Supersolid in Spin-Orbit-Coupled Bose Gases with Soft-Core Long-Range Interactions. *Phys. Rev. Lett.* 2018;121. <https://doi.org/10.1103/PhysRevLett.121.030404>.
- [35] Kartashov YV, Skryabin DV. Two-Dimensional Topological Polariton Laser. *Phys. Rev. Lett.* 2019;122. <https://doi.org/10.1103/PhysRevLett.122.083902>.

- [36] Lagaris IE, Likas A, Fotiadis DI. Artificial neural networks for solving ordinary and partial differential equations. *IEEE transactions on neural networks* 1998;9:987-1000. <https://doi.org/10.1109/72.712178>.
- [37] Blechschmidt J, Ernst OG. Three ways to solve partial differential equations with neural networks — A review. *GAMM-Mitteilungen* 2021;44. <https://doi.org/10.1002/gamm.202100006>.
- [38] Piette BMAG, Schroers BJ, Zakrzewski WJ. Dynamics of baby Skyrmions. *Nucl. Phys. B* 1995;439:205-235. [https://doi.org/10.1016/0550-3213\(95\)00011-g](https://doi.org/10.1016/0550-3213(95)00011-g).
- [39] Cho YM. Reinterpretation of Faddeev-Niemi knot in Skyrme theory. *Physics Lett. B* 2004;603:88-93. <https://doi.org/10.1016/j.physletb.2004.09.077>.
- [40] Malomed BA, Shnir Y, Zhilin G. Spontaneous symmetry breaking in dual-core baby-Skyrmion systems. *Phys. Rev. D* 2014;89. <https://doi.org/10.1103/PhysRevD.89.085021>.
- [41] Choi J, Kwon WJ, Shin Y. Observation of Topologically Stable 2D Skyrmions in an Antiferromagnetic Spinor Bose-Einstein Condensate. *Phys. Rev. Lett.* 2012;108. <https://doi.org/10.1103/PhysRevLett.108.035301>.
- [42] Zhang Y, Mao L, Zhang C. Mean-Field Dynamics of Spin-Orbit Coupled Bose-Einstein Condensates. *Phys. Rev. Lett.* 2012;108. <https://doi.org/10.1103/physrevlett.108.035302>.
- [43] Kartashov YV, Zezyulin DA. Stable Multiring and Rotating Solitons in Two-Dimensional Spin-Orbit-Coupled Bose-Einstein Condensates with a Radially Periodic Potential. *Phys. Rev. Lett.* 2019;122. <https://doi.org/10.1103/PhysRevLett.122.123201>.
- [44] Görlitz A, Vogels JM, Leanhardt AE, Raman C, Gustavson TL, Abo-Shaeer JR, et al. Realization of Bose-Einstein Condensates in Lower Dimensions. *Phys. Rev. Lett.* 2001;87. <https://doi.org/10.1103/PhysRevLett.87.130402>.

- [45] Malomed BA. (INVITED) Vortex solitons: Old results and new perspectives. *Physica D: Nonlinear Phenomena* 2019;399:108-137. <https://doi.org/10.1016/j.physd.2019.04.009>.
- [46] Chen Z, Li Y, Malomed BA. Josephson oscillations of chirality and identity in two-dimensional solitons in spin-orbit-coupled condensates. *Phys. Rev. Research* 2020;2. <https://doi.org/10.1103/PhysRevResearch.2.033214>.
- [47] Kanamoto R, Saito H, Ueda M. Quantum phase transition in one-dimensional Bose-Einstein condensates with attractive interactions. *Phys. Rev. A* 2003;67. <https://doi.org/10.1103/PhysRevA.67.013608>.
- [48] Becker C, Soltan-Panahi P, Kronjäger J, Dörscher S, Bongs K, Sengstock K. Ultracold quantum gases in triangular optical lattices. *New J. Phys.* 2010;12:065025. <https://doi.org/10.1088/1367-2630/12/6/065025>.
- [49] Dutta O, Gajda M, Hauke P, Lewenstein M, Lühmann D-S, Malomed BA, et al. Non-standard Hubbard models in optical lattices: a review. *Rep. Prog. Phys.* 2015;78:066001. <https://doi.org/10.1088/0034-4885/78/6/066001>.
- [50] Xu X-Q, Han JH. Emergence of Chiral Magnetism in Spinor Bose-Einstein Condensates with Rashba Coupling. *Phys. Rev. Lett.* 2012;108. <https://doi.org/10.1103/PhysRevLett.108.185301>.
- [51] Zhang X, Xia J, Zhou Y, Wang D, Liu X, Zhao W, et al. Control and manipulation of a magnetic skyrmionium in nanostructures. *Phys. Rev. B* 2016;94. <https://doi.org/10.1103/PhysRevB.94.094420>.
- [52] Bergé L. Wave collapse in physics: principles and applications to light and plasma waves. *Phys. Rep.* 1998;303:259-370. [https://doi.org/10.1016/s0370-1573\(97\)00092-6](https://doi.org/10.1016/s0370-1573(97)00092-6).
- [53] Kruglov VI, Volkov VM, Vlasov RA, Driks VV. Auto-waveguide propagation and the collapse of spiral light beams in nonlinear media. *J. Phys. A: Math. Gen.* 1988;21:4381-4395. <https://doi.org/10.1088/0305-4470/21/23/020>.